

Performance Analysis of Digital Flux-locked Loop Circuit with Different SQUID V - ϕ Transfer Curves for TES Readout System*

Nan Li,¹ Le-peng Li,¹ Meng-jie Song,¹ Hao-yu Li,¹ Xiang-xiang Ren,²
Yu-dong Gu,¹ Cong-zhan Liu,¹ Hai-feng Li,² He Gao,^{1,†} and Zheng-wei Li^{1,‡}

¹Key Laboratory of Particle Astrophysics, Institute of High Energy Physics,
CAS, 19B Yuquan Road, Shijingshan District, 100049, Beijing, China

²Key Laboratory of Particle Physics and Particle Irradiation (MOE),
Institute of Frontier and Interdisciplinary Science, Shandong University, Qingdao, Shandong, 266237, China

A superconducting quantum interference device (SQUID), functioning as a nonlinear response device, typically requires the incorporation of a flux-locked loop (FLL) circuit to facilitate linear amplification of the current signal transmitted through a superconducting transition-edge sensor (TES) across a large dynamic range. This work presents a reasonable model of the SQUID-FLL readout system, based on a digital proportional-integral-differential (PID) flux negative feedback algorithm. This work investigates the effect of V - ϕ shape on the performance of digital FLL circuits. Such as the impact factors of bandwidth, design limits of slew rate of the system and the influence of the shapes of SQUID V - ϕ curve. Furthermore, the dynamic response of the system to X-ray pulse signals with rise time ranging from 4.4~281 μ s and amplitudes ranging from 6~8 ϕ_0 was simulated. All the simulation results were found to be consistent with the existing mature theories, thereby validating the accuracy of the model. The results also provide a reliable modelling reference for the design of digital PID flux negative feedback and multiplexing SQUID readout electronic systems.

Keywords: TES, SQUID, Digital flux-locked loop, Readout system.

I. INTRODUCTION

As an ultra low-noise detector, a superconducting transition-edge sensor (TES) can achieve an energy resolution ranging from several to several tens of eV [1–3]. The energy resolution of TES is expected to be one to two orders of magnitude better than conventional HPGe semiconductor detectors [4, 5]. Therefore, TES can be applied in a variety of nuclear detection fields, such as X-ray/ γ -ray detection [6–13], dark matter [14, 15], double beta decay [16], cosmic microwave background (CMB) [14, 17], baryonic matter [18], nuclear medicine [19, 20], etc. To ensure a high signal-to-noise ratio of TES, a low-noise direct current superconducting quantum interference device (SQUID) is typically used to couple the TES current and then readout [21]. However, SQUID is a nonlinear device that can only guarantee linear amplification of the signal over a very small dynamic range. To enable the nonlinear SQUID to amplify the TES signal linearly over a larger dynamic range, it is necessary to construct a flux negative feedback lock loop (FLL) [22].

A significant benefit of employing a digital system to control a SQUID is the convenient manipulation of digitized signals. For example, the analog integrator and its reset circuit can be easily set up using just a few lines of code [23, 24]. The reset circuit not only automatically resets the position of

the V - ϕ curve prior to the SQUID lock, but also automatically adjusts the position of the FLL circuit working (locking) point. It has been demonstrated that digital FLL has the capacity to increase the dynamic input range of a SQUID to a substantial degree by using flux-quanta counting and dynamic field compensation (DFC) methods [25]. The noise spectral density measurement shows that the digital FLL system performs in a similar way to the analog FLL controller in previous work [26]. The digital FLL is now widely used in experiments such as magnetoencephalogram (MEG) [27], magnetocardiogram (MCG) [28], CMB [29], X-ray and γ -ray detection [30, 31]. Digital FLL is used in many time-division multiplexing (TDM) systems for TES readout and have detailed description of the digital feedback logic[32]. It is necessary to have fast response in X-ray detection, which requires the FLL to have a large slew rate[33], typically several μ s at 10 μ A [34], which is less than 2 ϕ_0 if the mutual inductance coefficient of SQUID coil is 5 μ A/ ϕ_0 . In CMB detection experiments, the design of digital FLL requires large bandwidth in order to improve multiplexing numbers of readout channels [35]. In order to understand the performance of the digital SQUID-FLL system and to design higher performance readout circuits, we simulate the functional upper limits of SQUID-FLL system. We also analyze the effect of shapes on the performance of digital FLL using three different shapes of SQUID V - ϕ curve models.

The paper is organized as follows: In Section II, a sinusoidal-like approximation is made to the SQUID flux response model, and the fundamentals of the digital SQUID-FLL circuit are introduced. In Section III, we conduct a comprehensive simulation analysis to validate the reliability of the model. This primarily entails simulations of the fundamental linear amplification readout function of the input magnetic flux signal, system bandwidth, and slew rate. Finally, the dynamic response of the system was simulated using pulse

* This work is supported by the National Key Research and Development Program of China (Grant No.2021YFC2203400, No.2022YFC2204900, No.2022YFC2204904, No.2020YFC2201704), National Natural Science Foundation of China No.12173040, Youth Innovation Promotion Association CAS 2021011 and Scientific Instrument Developing Project of the Chinese Academy of Sciences, Grant No.YJKYYQ20190065.

† Corresponding author, hgao@ihep.ac.cn.

‡ Corresponding author, lizw@ihep.ac.cn

signals that were designed to resemble actual TES pulse signals with varying rise time and amplitudes. This SQUID-FLL readout system model can provide reliable design references for digital flux negative feedback (DFB) readout and multiplexing SQUID readout systems. Section IV concludes the paper.

II. PRINCIPLE OF DIGITAL SQUID-FLL MODEL

A. Simplified SQUID transfer model

The circuit model of the SQUID-FLL is illustrated in Figure 1. It is comprised of a single-stage SQUID. The current signal flowing through the TES is coupled with the input coil L_{in} and converted into a magnetic flux signal ϕ_{in} . Although different designs for the SQUIDs exhibit varying responses

$$u_{err}(t) = A \sin \left(\frac{2\pi}{\phi_0} \left[i_{in}(t)M_{in} - \frac{u_o(t)M_{fb}}{R_{fb}} + \phi_{offset} \right] \right) G_1 \quad (1)$$

where ϕ_0 denotes the quantum magnetic flux. $i_{in}(t)$ is the TES signal through the input coil and the input flux is given by $\phi_{in} = i_{in}(t)M_{in}$. ϕ_{offset} is the magnetic flux bias applied to the input or feedback coils. $u_o(t)$ denotes the feedback voltage signal. R_{fb} denotes the feedback resistor and the feedback magnetic flux is given by $\phi_{fb} = \frac{u_o(t)M_{fb}}{R_{fb}}$. G_1 denotes the linear gain of the room low-noise preamplifier. A denotes the amplitude of the voltage across the SQUID. An offset voltage u_{offset} can also be introduced into the circuit to bias the preamplifier when tuning the lock point, as shown

to input magnetic flux ϕ_{in} , and all have common characteristics: the response of SQUID to ϕ_{in} is periodic and nonlinear, which resembles a quasi-sinusoidal curve [36]. Following magnetic flux locking, the error between the input and feedback magnetic flux is nearly zero, maintaining the total flux value in the SQUID at the working point. Theoretically, we only need to know the linear conversion coefficient of $dV_{SQUID}/d\phi_{in}$ at the lock point [37] but do not need to care any shape of the V - ϕ response curve of SQUID, where V_{SQUID} represents the voltage across SQUID. To prove this point, we simulate the FLL circuit for different SQUID flux response cases in Section III.

We simplify the SQUID V - ϕ transfer model to a standard sinusoidal function. Assuming that the mutual inductance coefficient of the SQUID input coil is M_{in} and the mutual inductance coefficient of the feedback coil is M_{fb} , the relationship between the error signal $u_{err}(t)$ and the input and feedback magnetic fluxes can be expressed as follows:

in Figure 1.

B. Principle of digital FLL

The fundamental structure of the FLL is the construction of a closed-loop negative flux feedback circuit based on operational amplifiers [38], as shown in the left part of Figure 1. By analyzing the current relationships contained within the green dashed line in Figure 1, we can derive the circuit equation relating the output digital signal $u_o(n)$ to the input error signal $u_{err}(n)$:

$$u_o(n) = - \left\{ \left(\frac{R_2}{R_1} + \frac{C_1}{C_2} \right) u_{err}(n) + \frac{\Delta t}{R_1 C_2} \sum_{i=0}^n u_{err}(i) + \frac{R_2 C_1}{\Delta t} [u_{err}(n) - u_{err}(n-1)] \right\} \quad (2)$$

where R_1 and C_1 are the input resistance and capacitance, respectively. R_2 and C_2 are the feedback resistance and capacitance, respectively. $P \equiv \left(\frac{R_2}{R_1} + \frac{C_1}{C_2} \right)$ is a proportional parameter. $I \equiv \frac{\Delta t}{R_1 C_2}$ is the integral parameter. $D \equiv \frac{R_2 C_1}{\Delta t}$ is the

differential parameter. Δt represents the digital sampling period. $u_{err}(i)$ denotes the i -th sampled error signal after amplification by G_1 . $u_{err}(n)$ is the average value of all sampled $u_{err}(i)$ in one frame as shown in Figure 2. $u_o(n)$ is the n -th output (feedback) signal. Similarly, by digitizing Equation 1, we obtain:

$$u_{err}(i) = A \sin \left(\frac{2\pi}{\phi_0} \left[i_{in}(i)M_{in} - \frac{u_o(n)M_{fb}}{R_{fb}} + \phi_{offset} \right] \right) G_1 \quad (3)$$

The primary objective of the PID algorithm design is to

calibration of the three aforementioned parameters. If these

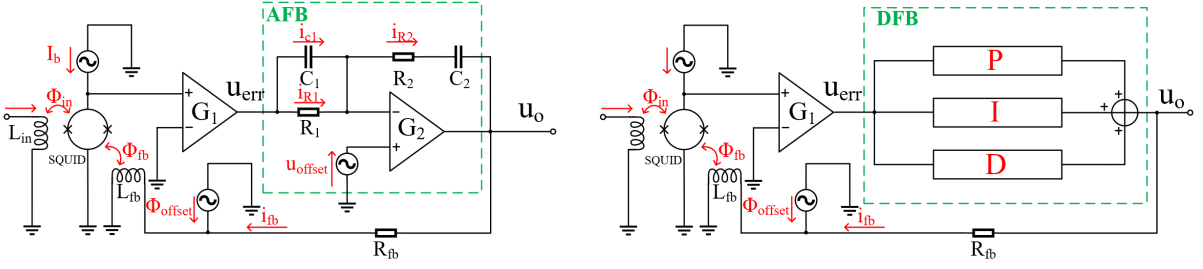


Fig. 1. SQUID-FLL readout circuit model. ϕ_{in} is the input flux signal and ϕ_{fb} is the feedback flux. G_1 is linear gain of room temperature preamplifier. ϕ_{offset} is the magnetic flux offset bias applied to the feedback coil here. u_{offset} is the voltage offset of the amplifier. The left figure shows the principle design of analog SQUID-FLL circuit. The right figure is the equivalent digital PID circuit. Analog feedback (AFB) and digital feedback (DFB) circuits are included in the green dashed lines.

parameters are not adequately calibrated, system oscillations can occur, which may lead to an extended time to lock (track) the signal or even a loss of lock.

III. DIGITAL SQUID-FLL PERFORMANCE ANALYSIS

A. Basic characterization of digital SQUID-FLL system

In our simulation, we emulated the typical conditions employed in laboratory tests, assuming that the SQUID is biased at a position with a substantial voltage swing prior to flux locking. The current through TES $i_{in}(i)$ serves as the input reference for the SQUID input coil L_{in} . The default parameters used in the simulation, unless otherwise specified, are listed in Table 1.

Table 1. Default simulation parameters of SQUID-FLL system.

Parameter	Value
Input signal type	Triangle Wave
Input signal frequency	23 Hz
Input signal amplitude	50 μ A
Testing time	50 ms
Digital sample rate	150 MSPS
Sample numbers per feedback	7
Mutual inductance of input coil $1/M_{in}$	28 μ A/ ϕ_0
Mutual inductance of feedback coil $1/M_{fb}$	38 μ A/ ϕ_0
Conversion coefficient $dV_{SQUID}/d\phi_{in}$ at lock point	3 mV/ ϕ_0
Input resistor R_1	100 Ω
Feedback resistor R_2	50 Ω
Input capacitor C_1	0 nF
Feedback capacitor C_2	1 nF
Feedback resistor R_{fb}	10 k Ω
Preamplifier gain G_1	100
Voltage amplitude across SQUID Array	700 μ V
Preamplifier voltage offset u_{offset}	0 μ V
Flux offset ϕ_{offset}	0 $\mu\phi_0$
Settle time t_{set}	0 ns

The rise time of TES's signals are typically from several μ s to several tens of ms [39, 40]. Consequently, the feedback algorithm design does not require consideration of future trend predictions. Consequently, in the default settings,

the input capacitance C_1 was set to 0, retaining only the P and I components. Considering the prospective system design, the digital sampling time was established at 150 MSPS, with seven points sampled in each frame. The frame clock (feedback frequency) was approximately 21.4 MHz, and the effective system Nyquist bandwidth is approximately 10.7 MHz. In digital feedback, the error signal from the current frame is used to compute the feedback signal for the next frame, which results in a delayed feedback loop. This process is analogous to TDM SQUID readout logic, with the exception of row selection [32, 41]. In this configuration, the frame frequency is equal to the row selection frequency in the TDM. The timing logic is illustrated in Figure 2. Average value of the error signal, $u_{err}(n)$, is calculated from the $u_{err}(i)$ to $u_{err}(i+6)$ values in the n -th frame. The feedback signal $u_o(n)$ is then calculated for the next frame. It should be noted that our model does not take into account other system delays, which typically amount to several hundred nanoseconds and may include transmission line delays. While these delays may reduce the system bandwidth, they do not impact the model's behaviour. Prior to the locking of the SQUID, it is essential to adjust the locking work point. Typically, in order to ensure linear amplification with no offset, the lock point is selected at the zero point of the input flux ($\phi_{in} = 0$) and the zero point of the output (feedback) flux ($\phi_{fb} = 0$). The initial error signal is set to 0. The bias signals ϕ_{offset} , u_{offset} and settle time t_{set} are also set to 0. The results of the feedback locking are shown in Figure 3. The absolute error signal does not exceed 10 $\mu\phi_0$, and the calculated relative error signal is less than 0.1 %.

The locking conditions were simulated under different flux and voltage offset conditions. In typical circumstances, the response of the input flux $dV_{SQUID}/d\phi_{in}$, near the SQUID locking point, must have the opposite polarity as the room temperature amplifier gain to ensure that the SQUID locking point is maintained. This is shown in Figures 4 (a) and (c). In the event that the polarity of the room temperature amplifier gain is identical to that of the SQUID response, a locking point offset phenomenon is observed, as illustrated in Figure 4 (b). In order to verify the independence of the FLL circuit from the shape of the SQUID V - ϕ response curve, as illustrated in Section II A, we simulate flux locking for differ-

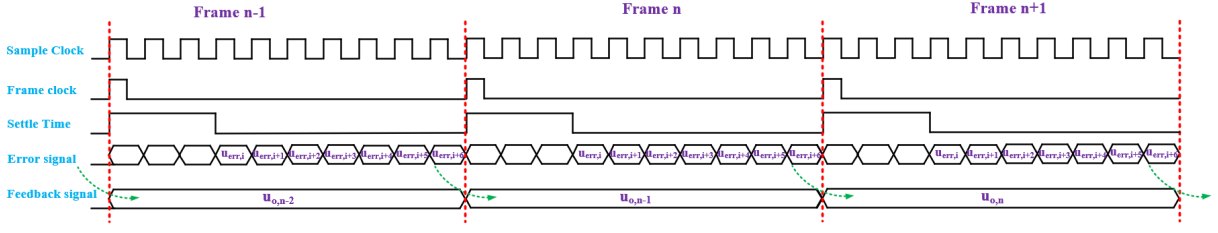


Fig. 2. Time logic of digital sample frequency and frame clock (feedback frequency). Sampled error signals $u_{err}(i)$ are used to calculate next frame feedback signal $u_o(n)$ based on PID algorithm.

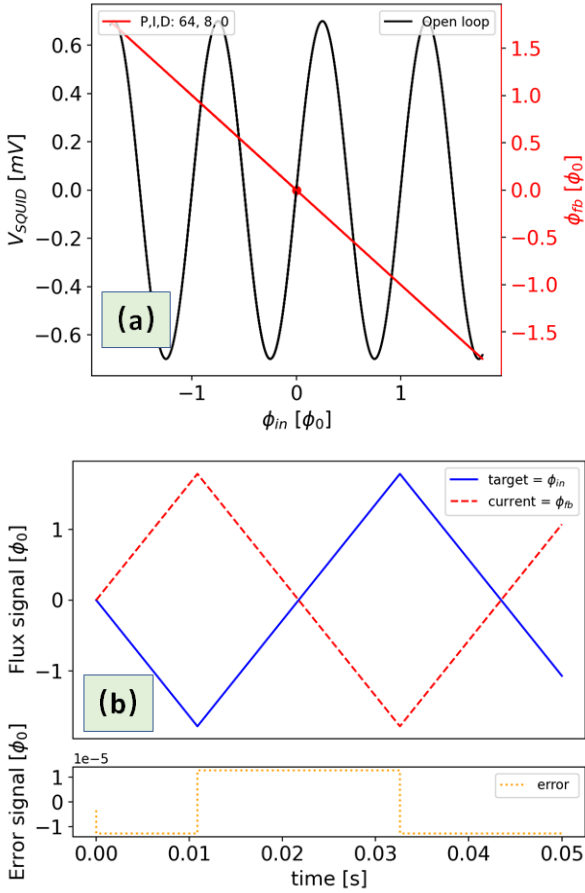


Fig. 3. Simulation result of SQUID-FLL model based on PID algorithm with low frequency triangle wave. (a) Black line show the relationship between output flux ϕ_{fb} and input flux ϕ_{in} without flux lock loop. Red line shows the locked linear gain with default PID parameters at lock point (red dot). All PID parameters on the legend are relative values calculated according to Table 1 and shifted 7 bits to the left. (b) ϕ_{fb} (red dashed line) tracks ϕ_{in} (blue solid line) in time domain after flux lock. The orange dotted line below shows the tracked flux error, which is less than $10 \mu\phi_0$.

B. Bandwidth and slew rate of digital SQUID-FLL system

When designing a SQUID-FLL circuit, it is essential to consider the rational design of the system bandwidth, particularly in multiplexing experiments. An FLL with a small bandwidth may result in distortion of the TES signal, whereas a larger bandwidth could introduce additional high-frequency noise, which would in turn affect the energy resolution of the TES. The effect of different feedback capacitors C_2 (integral component) and different shapes of V - ϕ transfer curves on the bandwidth was simulated, and the results are shown in Figure 6. In Figure 6, we consider the ideal case, without considering digital circuit delays ($t_{set} = 0$), as in analog FLL. All SQUID V - ϕ curves have same conversion coefficient $dV_{SQUID}/d\phi_{in}$ at the locking point and linear dynamic input range. The PID feedback is a time-domain simulation. By comparing it with the frequency-domain transfer function of the system, the correctness of the SQUID-FLL models can be verified. Based on frequency-domain transfer function [36], the theoretical 3 dB system bandwidth can be obtained:

$$f_c \approx \frac{V_\phi G_1 M_{fb}}{2\pi R_1 C_2 R_{fb}} \quad (4)$$

where $V_\phi = dV_{SQUID}/d\phi_{in}$ denotes the conversion coefficient at the locking point. For example, when $C_2 = 2$ nF, the calculated value for the critical frequency f_c based on Equation 4 is 628 kHz, which is in accordance with the results of different V - ϕ transfer models displayed in Figure 6. From Equation 4, it can be observed that a multitude of factors influence bandwidth, all of which are linearly correlated. In room temperature circuit design, the bandwidth can be determined by adjusting the preamp gain G_1 , input resistance R_1 , feedback capacitance C_2 , and feedback resistance R_{fb} . It is crucial to acknowledge that G_1 represents an ideal linear gain in the simulation. R_2 affects the DC gain of FLL, which is the discharge resistor for the C_2 , but does not determine the position of the f_c . In an actual design, the limitations of the operational amplifier's gain bandwidth product (GBP) must be considered. Therefore, this gain should not be excessively large for a system with a large bandwidth. Furthermore, in a practical design, system delays also reduce the bandwidth, necessitating the minimization of cable lengths. If the system delay is considered ($t_{set} \neq 0$), the system bandwidth should satisfy Equation 5 and the simulation results are shown in Fig-

ent shapes of the SQUID V - ϕ curve, as shown in Figure 5.

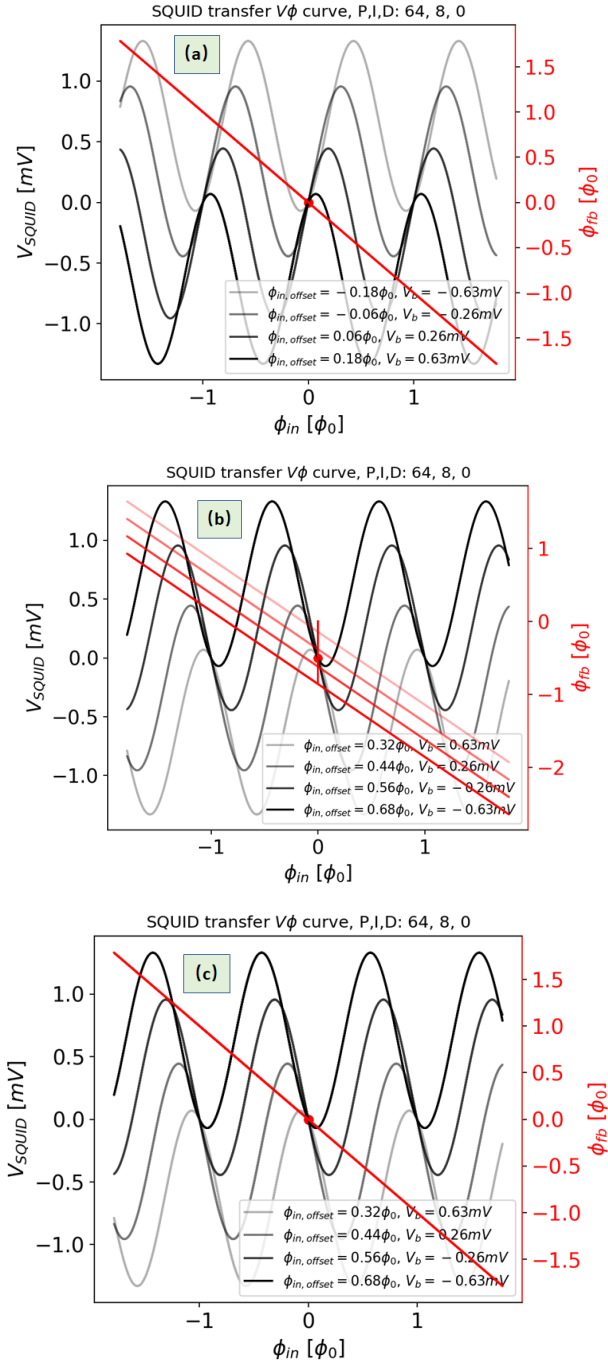


Fig. 4. Simulation results of SQUID-FLL model (red lines) under different flux offsets ϕ_{offset} and voltage offset u_{offset} (black lines). u_{offset} is added after G_1 .

(a) Results at different flux offset when room amplification gain is negative and $dV_{SQUID}/d\phi_{in} > 0$ at locking point. (b) Room amplification gain is negative but $dV_{SQUID}/d\phi_{in} < 0$ at locking point. Locking point offset appears. (c) Room amplification gain is positive and $dV_{SQUID}/d\phi_{in} < 0$ at locking point.

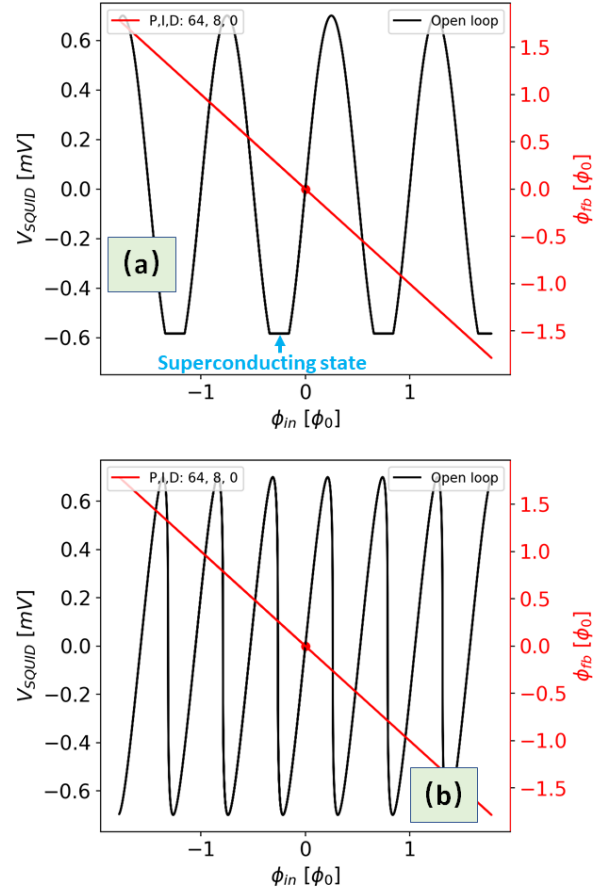


Fig. 5. Simulation results of SQUID-FLL (red lines) under varying SQUID V - ϕ response. (a) SQUID lock status at small bias current. The superconducting state exists at this moment. (b) Lock status at asymmetric response.

ure 7. t_{sp} is the ADC sampling period and N_{sp} is the number of samples. t_{fm} is the frame period.

$$f_c \approx \frac{V_\phi G_1 M_{fb} N_{sp} t_{sp}}{2\pi R_1 C_2 R_{fb} t_{fm}} \quad (5)$$

Further investigation was conducted on the system slew rate $\partial\phi_{fb}/\partial t$. When the bandwidth is sufficiently large but the slew rate is too small, it can also lead to signal distortion. The system slew rate is determined jointly by the bandwidth, the input range ϕ_{lin} of the SQUID's open-loop linear gain, and the design of the FLL integral parameter, and is independent of frequency [37]. This relationship can be expressed as follows:

$$\frac{\partial\phi_{fb}}{\partial t} = \frac{\phi_{lin} N_{sp} t_{sp}}{2R_1 C_2 t_{fm}} \quad (6)$$

In our SQUID transmission model, $\phi_{lin} \approx 0.3 \phi_0$, as shown on the top of Figure 6. Based on Equation 6, we calculated $\partial\phi_{fb}/\partial t \approx 1.5 \phi_0/\mu s$. The simulated result ($t_{set}=0$) was approximately $1.5 \phi_0/\mu s$, as shown in Figure 8. When the signal rise time exceed $1.6 \mu s$, the FLL is unable to accurately

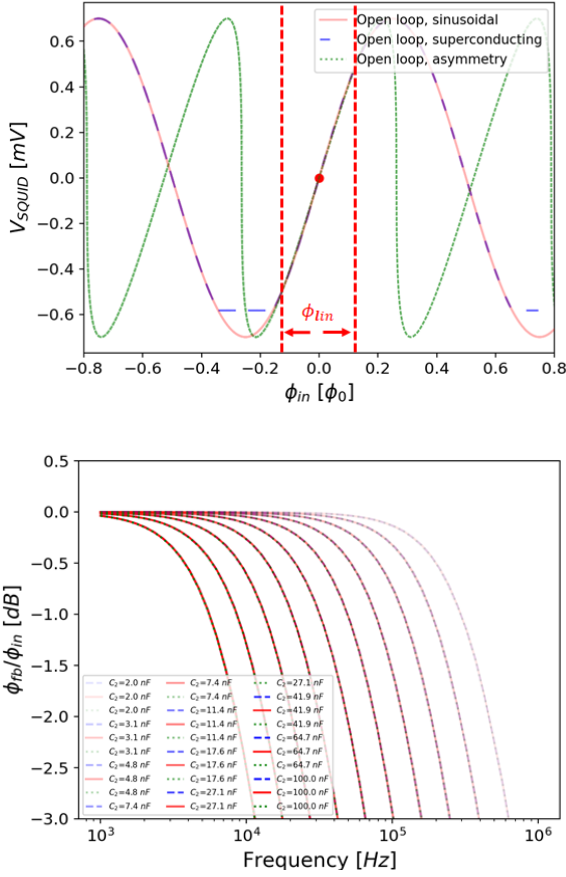


Fig. 6. SQUID-FLL system bandwidth simulation. The top figure shows the same open-loop linear gain input range ϕ_{lim} for three different shapes of $V-\phi$ response. The red solid line is the sinusoidal-like model. The blue dashed line is the small bias model with superconducting state. The green dotted line is the asymmetrical model. The bottom figure shows the bandwidth with different feedback capacitor C_2 for three varying shapes of $V-\phi$ curves, which prove that $V-\phi$ responses of different shapes have equivalent bandwidth when they have same V_ϕ conversion coefficient at the locking point.

track the signal, resulting in distortion. It can be seen that when the SQUID transfer model is different, the shape of the tracked signal is different when distortion appears. But the value of the slew rate is same. All signals are distorted at rise times less than $1.6 \mu s$, which is independent of the shape of the SQUID transfer model. For digital FLL, the slew rate decreases when the frame frequency is reduced, as shown in Figure 9. In theory, to track a faster signal, one can adjust the integration parameters, feedback resistance and so forth to modify the bandwidth. According to equations 5 and 6, the ideal linear relationship between slew rate and bandwidth is shown in Figure 10.

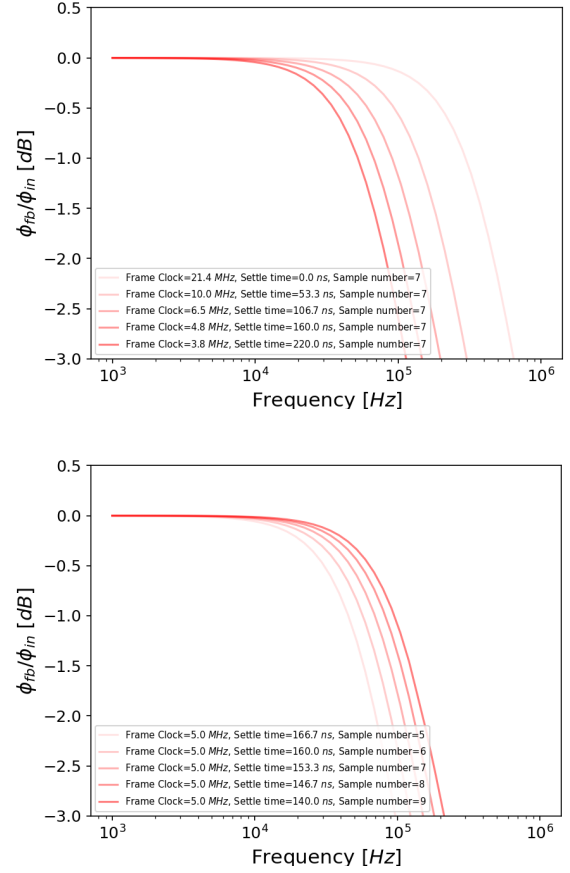


Fig. 7. Simulation results of SQUID-FLL under varying settle time. The top figure shows the bandwidth increases with the frame rate when N_{sp} is constant. The bottom figure shows the bandwidth increases with N_{sp} when the frame rate is constant.

C. Noise contribution in digital FLL system

The TES detector has a high energy resolution mainly due to its small thermal noise at low temperatures. In the experiment, the noise is mainly comprised of TES Johnson noise and thermal fluctuation noise (TFN) [42]. The thermal noise of SQUID and the voltage noise of preamplifier mainly constitute the system's high-frequency noise. For digital FLL circuits, the quantization noise of the ADC and DAC devices also affects the signal-to-noise ratio (SNR). The noise spectral density $S(f)$ of ADC or DAC should satisfy Equation 7.

$$S(f) = \frac{q}{\sqrt{12}} \frac{1}{\sqrt{BW}} \quad (7)$$

q is the least number bit (LSB) voltage of ADC or DAC. BW is the Nyquist bandwidth of the system. We can calculate the equivalent current noise density of ADC $S_{I,ADC}(f)$ and DAC $S_{I,DAC}(f)$ refer to the input coil of SQUID according to Equation 8 and 9.

$$S_{I,ADC}(f) = \frac{S_{ADC}(f)}{G_1 V_\phi M_{in}} \quad (8)$$

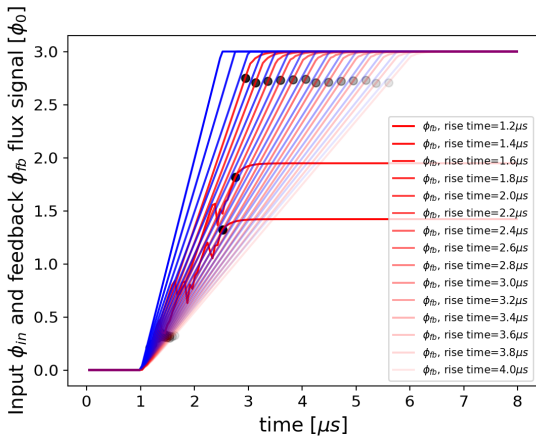
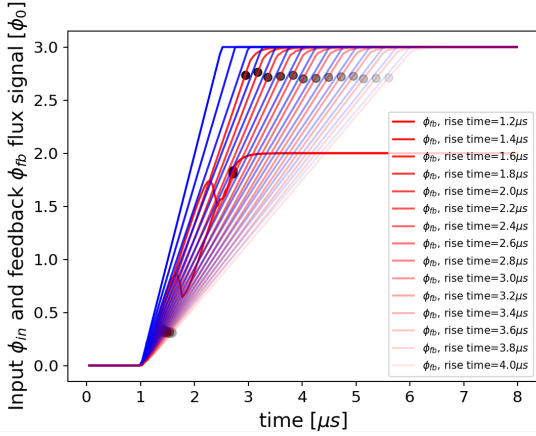


Fig. 8. SQUID-FLL system slew rate simulation. The top figure shows the same maximum slew rate of SQUID-FLL system is about $1.6 \phi_0/\mu\text{s}$ when the SQUID transfer functions are sinusoidal-like model or small bias model with superconducting state. The rise time of ϕ_{fb} (red line) is about $1.6 \mu\text{s}$ and the amplitude of ϕ_{fb} is up to $3 \phi_0$ without distortion. Rise time is from 10 % to 90% amplitude of signal. The bottom figure shows the same maximum slew rate of SQUID-FLL system based on asymmetrical model.

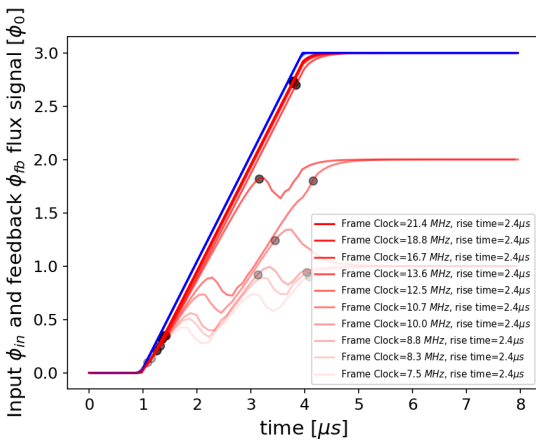


Fig. 9. Tracking $2.4 \mu\text{s}$, $3 \phi_0$ signals at different frame rates. The signal is distorted when the frame rate is reduced to 12.5MHz.

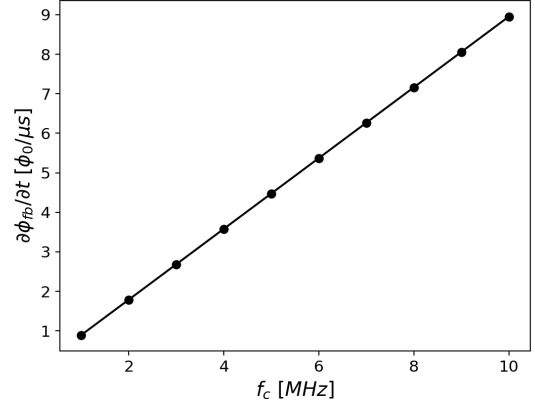


Fig. 10. The ideal relationship between SQUID-FLL system slew rate $\partial\phi_{fb}/\partial t$ and cutoff frequency f_c .

$$S_{I,DAC}(f) = \frac{S_{DAC}(f)M_{fb}}{R_{fb}M_{in}} \quad (9)$$

Where $S_{ADC}(f)$ and $S_{DAC}(f)$ represents the intrinsic noise of ADC and DAC. For example, the equivalent current noise of a 16-bit ADC with 2 V full scale range is $0.8 \text{ pA}/\sqrt{\text{Hz}}$ refers to the input coil of SQUID, which is far less than the noise of TES (generally several tens to hundreds $\text{pA}/\sqrt{\text{Hz}}$). The equivalent noise of a 16-bit DAC is $0.6 \text{ pA}/\sqrt{\text{Hz}}$ when the feedback resistor is 10 k Ω as shown in Table 1. Thus, it is better to choose a large feedback resistor and high-resolution ADC and DAC for digital FLL.

D. X-ray pulse signal response

Considering that the TES used for X-ray detection has a fast response time of the order of a few microseconds to several hundred microseconds, we use a small pulse signal comprising white noise as input to simulate the response process of the X-ray TES[42]. If the Nyquist noise bandwidth is 1 MHz, the noise of the TES system was set to $50 \text{ pA}/\sqrt{\text{Hz}}$ at 1 kHz and an RMS value of 22 μA (refer to the SQUID input coil), which is based on our testing results [43]. We use the sinusoidal-like SQUID-FLL model to demonstrate effective tracking of pulses with varying rise time, as illustrated in Figure 11 (a). Furthermore, a simulation was performed in which the rise time was set at $4.3 \mu\text{s}$ while the pulse amplitude was increased. The results of this simulation are shown in Figure 11 (b). Distortion occurs when the signal amplitude exceeds $7.8 \phi_0$. The corresponding slew rate is approximately $1.45 \phi_0/\mu\text{s}$, which is consistent with the simulation results shown on the right side of Figure 8.

IV. CONCLUSION

A comprehensive behavioral simulation of the SQUID-FLL circuit was performed using different SQUID models in

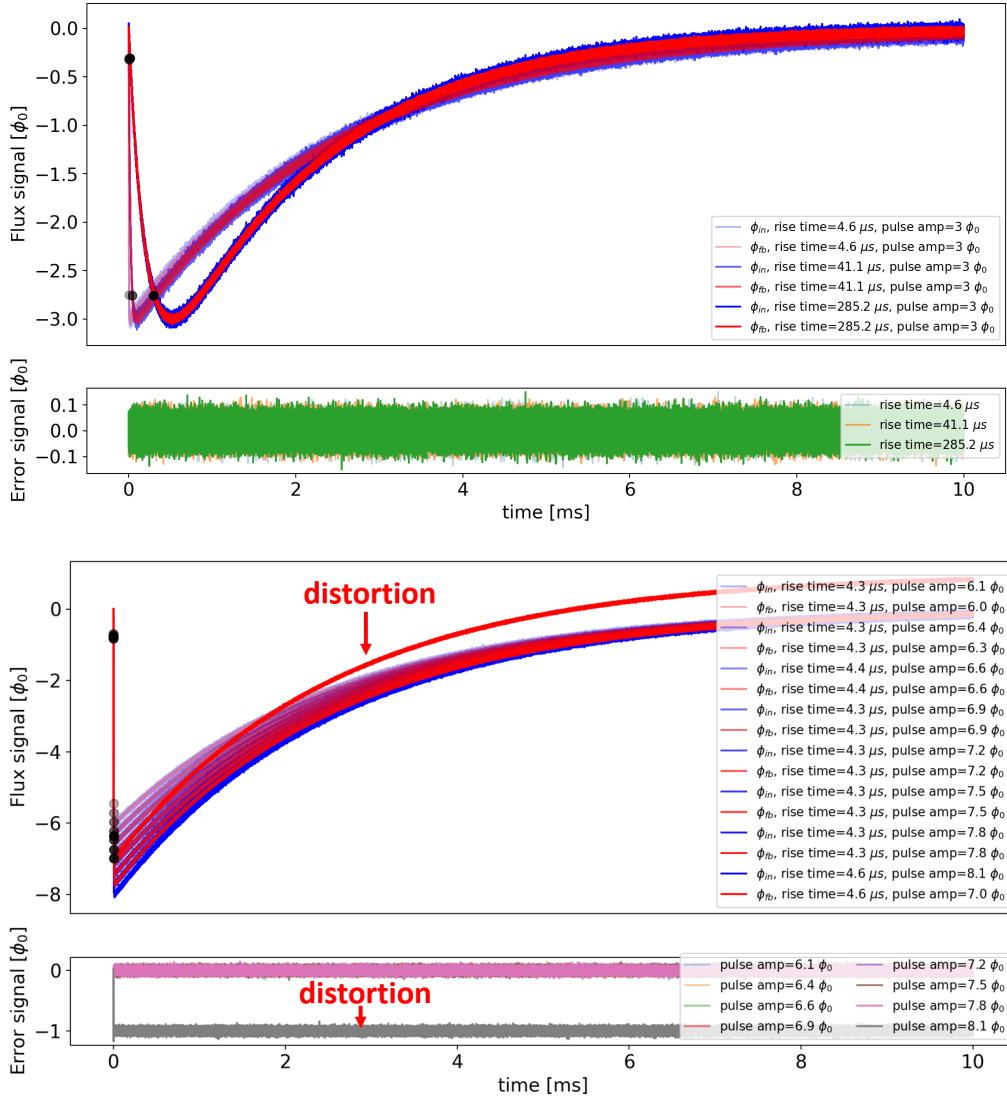


Fig. 11. Simulation of X-ray pulses with 22 μA RMS noise. (a) Signal (blue lines) can be tracked well (red lines) when the rise time is not less than 4.3 μs and the amplitude of pulse is 3 ϕ_0 . (b) When the amplitude is larger than 7.8 ϕ_0 and the rise time is about 4.3 μs , signal distortion appears.

conjunction with the principles of digital PID magnetic flux feedback. We demonstrate that the design of the FLL does not depend on the shape of the SQUID V - ϕ response by simulating SQUID transfer function models with three different shapes. A comprehensive list of parameters that must be considered when designing the SQUID-FLL system is presented in Table 1. Common scenarios of locking point adjustments during laboratory tuning were analyzed. The primary factors influencing the design of the system bandwidth f_c were ex-

amined, thereby providing valuable references for the design of SQUIDs and room readout electronics. Finally, the upper limit of the slew rate of the system was thoroughly analyzed, and it was found to be approximately 1.5 $\phi_0/\mu s$ under default parameters in our model. The tracking capability of the system was validated with simulated X-ray pulse signals with different rise time (4.4 to 281 μs) and amplitudes (6 to 8 ϕ_0). We hope that these simulation results will serve as a reference for the design of high-performance digital PID flux feedback electronic and multiplexing readout systems.

[1] Davide Vaccaro et al. System performance of a cryogenic test-bed for the time-division multiplexing readout for the

- Telescopes, Instruments, and Systems*, 10(4):046002–046002, 2024. DOI: 10.48550/arXiv.2409.05643.
- [2] Jiejia Liu et al. Preliminary design of detector assembly for dixe. *Journal of Low Temperature Physics*, 216(1):273–284, Jul 2024. DOI: 10.1007/s10909-024-03131-z.
- [3] Paul Szypryt et al. A tabletop x-ray tomography instrument for nanometer-scale imaging: Demonstration of the 1,000-element transition-edge sensor subarray. *IEEE Transactions on Applied Superconductivity*, 33(5):1–5, 2023. DOI: 10.1109/TASC.2023.3256343.
- [4] Yan Li, WenDa Huang, Shuanghui Shi, Jiahui Gu, Jingyi Liu, Xiaohan Yu, and Jiping Zeng. The level structure of 76se from 76br γ -decay. *Nuclear Science and Techniques*, 9(4):199–208, 1998. Web: <http://www.nst.sinap.ac.cn/article/id/5568>.
- [5] Weifan Yang, Zhizheng Zhao, Zongwei Li, and Wantong Mou. New gamma rays from decay of 189 w. *Nuclear Science and Techniques*, 6(4):222–224, 1995. Web: <https://api.semanticscholar.org/CorpusID:94061252>.
- [6] Luciano Gottardi and Kenichiro Nagayashi. A review of x-ray microcalorimeters based on superconducting transition edge sensors for astrophysics and particle physics. *Applied Sciences*, 11(9):3793, 2021. DOI: 10.3390/app11093793.
- [7] Joel N Ullom and Douglas A Bennett. Review of superconducting transition-edge sensors for x-ray and gamma-ray spectroscopy. *Superconductor Science and Technology*, 28(8):084003, 2015. DOI: 10.1088/0953-2048/28/8/084003.
- [8] Zhang Shuo, Cui Wei, Jin Hai, Chen Liu-Biao, Wang Jun-Jie, Wu Wen-Tao, Wu Bing-Jun, Xia Jing-Kai, Song Yan-Ru, Yang Jin-Ping, et al. Development of basic theory and application of cryogenic x-ray spectrometer in light sources and x-ray satellite. *Acta Physica Sinica*, 70(18), 2021. DOI: 10.7498/aps.70.20210350.
- [9] Zhen Wang, Chao Feng, Qiang Gu, Li-Hua Yu, and Zhen-Tang Zhao. Generation of double pulses at the shanghai soft x-ray free electron laser facility. *Nuclear Science and Techniques*, 28(3):28, 2017. DOI: 10.1007/s41365-017-0188-9.
- [10] Jens Uhlig, WB Doriese, JW Fowler, DS Swetz, C Jaye, DA Fischer, CD Reintsema, DA Bennett, LR Vale, Ujjwal Mandal, et al. High-resolution x-ray emission spectroscopy with transition-edge sensors: present performance and future potential. *Journal of synchrotron radiation*, 22(3):766–775, 2015. DOI: 10.1107/S1600577515004312.
- [11] William B Doriese, Peter Abbamonte, Bradley K Alpert, DA Bennett, EV Denison, Y Fang, DA Fischer, CP Fitzgerald, JW Fowler, JD Gard, et al. A practical superconducting-microcalorimeter x-ray spectrometer for beamline and laboratory science. *Review of Scientific Instruments*, 88(5), 2017. DOI: 10.1063/1.4983316.
- [12] Shuo Zhang, JingKai Xia, WenTao Wu, YanRu Song, BingJun Wu, and Zhi Liu. Tes-based x-ray spectrometer developed for shine project. In *Eighth Symposium on Novel Photoelectronic Detection Technology and Applications*, volume 12169, pages 381–385. SPIE, 2022. DOI: 10.1117/12.2622288.
- [13] Joseph W Fowler, Galen C O’Neil, Bradley K Alpert, Douglas A Bennett, Ed V Denison, WB Doriese, Gene C Hilton, Lawrence T Hudson, Young-II Joe, Kelsey M Morgan, et al. Absolute energies and emission line shapes of the l x-ray transitions of lanthanide metals. *Metrologia*, 58(1):015016, 2021. DOI: 10.1088/1681-7575/abd28a.
- [14] Junsong Cang, Yu Gao, and Yin-Zhe Ma. Probing dark matter with future cmb measurements. *Physical Review D*, 102(10):103005, 2020. DOI: 10.1103/PhysRevD.102.103005.
- [15] Philippe Camus, Jonathan Corbett, Sean Crawford, Koby Der-ing, Eleanor Fascione, Gilles Gerbier, Richard Germond, Muad Ghaith, Jeter Hall, Ziqing Hong, et al. Cute: A cryogenic underground test facility at snolab. *Frontiers in Physics*, 11:1319879, 2024. DOI: 10.3389/fphy.2023.1319879.
- [16] G Bratrud, CL Chang, R Chen, E Cudmore, E Figueroa-Feliciano, Z Hong, KT Kennard, S Lewis, M Lisovenko, LO Mateo, et al. First demonstration of a tes based cryogenic li₂ moo₄ detector for neutrinoless double beta decay search. *arXiv preprint arXiv:2406.02025*, 2024. DOI: 10.1140/epjc/s10052-025-13844-4.
- [17] Yongping Li, Yang Liu, Si-Yu Li, Hong Li, and Xinmin Zhang. Tibet’s ali: a new window to detect the cmb polarization. *arXiv preprint arXiv:1709.09053*, 2017. DOI: 10.48550/arXiv.1709.09053.
- [18] Wei Cui, JN Bregman, MP Bruijn, L-B Chen, Y Chen, C Cui, T-T Fang, B Gao, H Gao, J-R Gao, et al. Hubs: a dedicated hot circumgalactic medium explorer. In *Space Telescopes and Instrumentation 2020: Ultraviolet to Gamma Ray*, volume 11444, pages 470–481. SPIE, 2020. DOI: 10.1117/12.2560871.
- [19] Feng Xie, Xiaobing He, Wengang Jiang, Zhanying Chen, Quanlin Shi, and Yongfu Chang. Determination of absolute gamma-ray emission probabilities for 88 kr. *Nuclear Science and Techniques*, 22(5):304–306, 2011. DOI: 10.13538/j.1001-8042/nst.22.304-306.
- [20] Min Lin, Yundong Chen, Ying Cui, Kesheng Chen, Huazhi Li, Zhenhong Xiao, T Kojima, Z Peimel-Stuglik, and S Fabisiak. Dose inter-comparison studies for 60 co gamma-ray and electron beam irradiation in the year 2002. *Nuclear Science and Techniques*, 15(3):166–173, 2004. Web: <http://www.nst.sinap.ac.cn/article/id/1711>.
- [21] Wentao Wu et al. Development of series squid array with on-chip filter for tes detector. *Chinese Physics B*, 31(2):028504, 2022. DOI: 10.1088/1674-1056/ac2b91.
- [22] Dietmar Drung et al. Low-noise ultra-high-speed dc squid readout electronics. *Superconductor Science and Technology*, 19(5):S235, 2006. DOI: 10.1088/0953-2048/19/5/S15.
- [23] Inseob Hahn and Mark Weilert. Digital signal processor-based dc superconducting quantum interference device controller. *Review of Scientific Instruments*, 72(4):2203–2206, 04 2001. DOI: 10.1063/1.1350646.
- [24] Ludwig et al. Versatile high performance digital squid electronics. *IEEE transactions on applied superconductivity*, 11(1):1122–1125, 2001. DOI: 10.1109/77.919545.
- [25] Dietmar Drung. High-tc and low-tc dc squid electronics. *Superconductor science and technology*, 16(12):1320, 2003. DOI: 10.1088/0953-2048/16/12/002.
- [26] B. Limketkai et al. A digital squid controller. *Physica B: Condensed Matter*, 329-333:1506–1507, 2003. Proceedings of the 23rd International Conference on Low Temperature Physics.
- [27] Jiri Vrba and Stephen E. Robinson. Signal processing in magnetoencephalography. *Methods*, 25(2):249–271, 2001. DOI: 10.1006/meth.2001.1238.
- [28] Daisuke Oyama et al. Development of digital fll system for squid using double counter method. *IEEE transactions on magnetics*, 42(10):3539–3541, 2006. DOI: 10.1109/T-MAG.2006.879162.
- [29] Kevork N. Abazajian et al. CMB-S4 Science Book, First Edition. 10 2016. DOI: 10.48550/arXiv.1610.02743.
- [30] Didier Barret et al. The athena x-ray integral field unit: a consolidated design for the system requirement review of the preliminary definition phase. *Experimental Astronomy*,

- 55(2):373–426, Apr 2023. DOI: [10.1007/s10686-022-09880-7](https://doi.org/10.1007/s10686-022-09880-7).
- [31] Shuo Zhang et al. Transition edge sensor-based detector: from x-ray to γ -ray. *Nuclear Science and Techniques*, 33(7):84, Jul 2022. DOI: [10.1007/s41365-022-01071-5](https://doi.org/10.1007/s41365-022-01071-5).
- [32] Carl D Reintsema et al. Prototype system for superconducting quantum interference device multiplexing of large-format transition-edge sensor arrays. *Review of Scientific Instruments*, 74(10):4500–4508, 2003. DOI: [10.1063/1.1605259](https://doi.org/10.1063/1.1605259).
- [33] Malcolm Durkin, Galen C O’Neil, William B Doriese, Johnathon D Gard, Gene C Hilton, Jozsef Imrek, N Ortiz, Carl D Reintsema, Robert W Stevens, Daniel S Swetz, et al. A predictive control algorithm for time-division-multiplexed readout of tes microcalorimeters. *Journal of Low Temperature Physics*, 199(1):275–280, 2020.
- [34] Caroline A Kilbourne, Simon R Bandler, Ari-D Brown, James A Chervenak, Eneotali Figueroa-Feliciano, Fred M Finkbeiner, Naoko Iyomoto, Richard L Kelley, F Scott Porter, and Stephen J Smith. Uniform high spectral resolution demonstrated in arrays of tes x-ray microcalorimeters. In *UV, X-Ray, and Gamma-Ray Space Instrumentation for Astronomy XV*, volume 6686, pages 52–61. SPIE, 2007. DOI: [10.1117/12.734830](https://doi.org/10.1117/12.734830).
- [35] W. B. Doriese et al. Developments in time-division multiplexing of x-ray transition-edge sensors. *Journal of Low Temperature Physics*, 184(1):389–395, Jul 2016. DOI: [10.1007/s10909-015-1373-z](https://doi.org/10.1007/s10909-015-1373-z).
- [36] Dietmar Drung and Michael Mück. Squid electronics. In J. Clarke and A.I. Braginski, editors, *The SQUID Handbook Vol. 1*, pages 127–170. Wiley-VCH, 2004. DOI: [10.1002/3527603646](https://doi.org/10.1002/3527603646).
- [37] Dietmar Drung. High-performance dc squid read-out electronics. *Physica C: Superconductivity*, 368(1):134–140, 2002. DOI: [10.1016/S0921-4534\(01\)01154-6](https://doi.org/10.1016/S0921-4534(01)01154-6).
- [38] D Drung et al. Improved direct-coupled dc squid read-out electronics with automatic bias voltage tuning. *IEEE transactions on applied superconductivity*, 11(1):880–883, 2001. DOI: [10.1109/77.919485](https://doi.org/10.1109/77.919485).
- [39] Stephen Thurgate and Terrence Jach. Processing pulses from tes microcalorimeter x-ray detectors. *Nuclear Instruments and Methods in Physics Research Section A: Accelerators, Spectrometers, Detectors and Associated Equipment*, 1014:165707, 2021. DOI: [10.1016/j.nima.2021.165707](https://doi.org/10.1016/j.nima.2021.165707).
- [40] Y. Yagi et al. Performance of tes x-ray microcalorimeters designed for 14.4-keV solar axion search. *Journal of Low Temperature Physics*, 211(5):255–264, Jun 2023. DOI: [10.1007/s10909-023-02942-w](https://doi.org/10.1007/s10909-023-02942-w).
- [41] Elia Stefano Battistelli et al. Functional description of read-out electronics for time-domain multiplexed bolometers for millimeter and sub-millimeter astronomy. *Journal of Low Temperature Physics*, 151:908–914, 2008. DOI: [10.1007/s10909-008-9772-z](https://doi.org/10.1007/s10909-008-9772-z).
- [42] Kent D. Irwin and Gene C. Hilton. Transition-edge sensors. In Chr. Enss, editor, *Cryogenic Particle Detection*, volume 99 of *Topics in Applied Physics*, pages 63–152. Springer, 2005. DOI: [10.1007/b12169](https://doi.org/10.1007/b12169).
- [43] N. Li et al. A configurable ultra-low noise current source for transition-edge sensor characterization. *Journal of Instrumentation*, 19(05):P05038, may 2024. DOI: [10.1088/1748-0221/19/05/P05038](https://doi.org/10.1088/1748-0221/19/05/P05038).